

# Chapter 5

## Light-Nanomatter Chiral Interaction in Optical-Force Effects



Hajime Ishihara, Masayuki Hoshina, Hidemasa Yamane,  
and Nobuhiko Yokoshi

**Abstract** The interaction between chiral objects and chiral environment is a fundamental topic in various research domains such as chemistry, material physics, optics, and bioscience. Particularly, the chiral interplay between light and nanostructures has been a fascinating topic because of its potential applications in chemical analyses, molecular sensing, novel light sources, and optical manipulations with high degree of freedom. Further, the study of relevant subjects will shed light on the unconventional fundamentals of light–matter interaction where the nanoscale spatial correlation between the light and matter geometries plays an essential role therein, which is beyond the conventional picture of optical response based on the long wavelength approximation of light or dipole approximation of matter systems. In this chapter, we introduce the recent theoretical studies on light–nanomatter chiral interactions, focusing on two topics in optical-force effects. The first topic is a scheme to measure the circular dichroism (CD) of the chiral near field in the vicinity of metallic nanostructures. This scheme evaluates the CD by measuring the optical force that acts on the probe tip with the circularly polarized lights irradiated. The second topic is the proposal of the rotational-motion control of nanoparticles in a nanoscale area by using the optical force generated through the interaction between a chiral light field (optical vortex) and a metallic nanocomplex. The results revealed the unique role of the optical force in the studies of the light–nanomatter chiral interaction.

---

H. Ishihara (✉)

Department of Materials Engineering Science, Osaka University,  
1-3 Machikaneyama-cho, Toyonaka, Osaka 560-8531, Japan  
e-mail: [ishi@mp.es.osaka-u.ac.jp](mailto:ishi@mp.es.osaka-u.ac.jp)

Department of Physics and Electronics, Osaka Prefecture University,  
1-1 Gakuen-cho, Naka-ku, Sakai, Osaka 599-8531, Japan

Quantum Information and Quantum Biology Division, Institute for Open  
and Transdisciplinary Research Initiatives, Osaka University, 1-3 Machikaneyama-cho,  
Toyonaka, Osaka 560-8531, Japan

M. Hoshina · H. Yamane · N. Yokoshi  
Department of Physics and Electronics, Osaka Prefecture University,  
1-1 Gakuen-cho, Naka-ku, Sakai, Osaka 599-8531, Japan

© Springer Nature Switzerland AG 2021

E. Kamenetskii (ed.), *Chirality, Magnetism and Magnetolectricity*,  
Topics in Applied Physics 138,  
[https://doi.org/10.1007/978-3-030-62844-4\\_5](https://doi.org/10.1007/978-3-030-62844-4_5)

## 5.1 Introduction

Chirality is the property that the spatial geometries of matters, fields, and motions cannot be identical to their mirror images. There exist various kinds of chiral structures or phenomena for different objects such as nucleons, amino acids, and liquid crystals. The chiral interaction between light and matter, especially, has been an important subject in various research domains. For example, the circular dichroism (CD) of materials, which is a difference between the absorptions of left- and right-circularly polarized lights, has been a standard measure of matter chirality for a long time. However, the chirality of light is also affected by the interaction with matter. Optical rotation and circularly polarized luminescence are typical examples. Recently, chiral interaction has been applied to the generation of light with orbital angular momentum, sometimes referred to as optical vortex. Accordingly, chiral interactions have been one of the fundamental principles in germinating, probing, and designing the nature and the function of matter and light.

Recently, the research on chiral interactions has taken a new step because of the rapid development of nanofabrication technologies and characterization techniques of few-molecule systems. For example, the high-accuracy fabrication of metallic structures enables us to control the localized electric field in nanoscale areas owing to localized surface plasmon (LSP). By using LSP effect, we can realize circularly polarized fields with significantly reduced pitch of polarization rotation, i.e., the so-called superchiral fields [1]. In the past 20 years, various nanostructures have been reported to generate superchiral fields [2–9]. In addition, the CD signal of the plasmonic near field was measured via photon scanning tunneling microscopy or near-field scanning optical microscopy (SNOM) [10–13]. Superchiral fields boost the molecular CD signal, although the signals of individual molecules, such as proteins, DNA, and carbon nanotubes, are generally small. The superchiral field is expected to be a promising tool for performing the sensitive enantioselective detections of chiral molecules [14–17]. Another interesting application of LSP is the conversion between the spin angular momentum and orbital angular momentum. A plane wave light with circularly polarization has spin angular momentum, but not orbital angular momentum. However, when it is radiated onto metallic nanocomplexes, the induced plasmonic near field can exhibit optical current with orbital angular momentum [18]. The optical response of a matter manifests not only as optical outputs but also as a mechanical force exerted on the matter system. Therefore, the plasmonic near field with the nanoscale radius of gyration is expected to enhance the degree of freedom to manipulate the center-of-mass motion of nanoobjects.

For the analyses of light–matter chiral interactions, we should note that the conventional scheme of light–matter interaction based on the long wavelength approximation (LWA) of light or dipole approximation (DA) of matter does not work because the chiral nanostructures have a nanoscale polarization configuration. Moreover, the chiral light induces non-dipole polarization structures of matter systems. Thus, the non-local response is important in nanoscale chiral light–matter interactions, in which the nanoscale spatial correlation between light and matter plays an essential role.

Anomalous optical responses of nanostructures due to the nonlocal characteristics of the response were theoretically proposed [19, 20], and have been experimentally demonstrated as the giant nonlinear response of quadrupole excitons [21], the optical forbidden electronic transition of a single-wall carbon nanotube [22], and the ultra-short radiative decay time in the femtosecond regime [23, 24], etc. Chiral interaction of light–nanomaterials is another frontier wherein the nonlocal optical response induces anomalous effects beyond LWA or DA.

Based on the nonlocal scheme, we have focused on the mechanical force (optical force) associated with the chiral interaction between plasmonic near-field and matter. Specifically, the following two issues are introduced. The first issue is the three-dimensional (3D) near-field CD during the optical-force measurement. As aforementioned, the aperture-type SNOM is a powerful tool to unveil the chiral near field [13]. However, it is difficult to elucidate the 3D structure of a superchiral field, especially around the edges of metallic structures, as the longitudinal component is dominant there. We show that if we measure the optical-force between the dipoles induced on the sample and the probe tip irradiated by light, we can observe the 3D distribution of the electric-field intensity to evaluate the 3D near-field CD (3D NF-CD). The other issue is the optical manipulation of nanoparticles (NPs) near metallic nanocomplexes with a high degree of freedom. We show that the flexible rotational optical manipulation, such as the rotation control in nanoscale area and switching of the rotational direction, of nanoobjects can be achieved. This means that all the basic elements of nanoobject-motion control (i.e., pushing, pulling, and rotating) are realized in principle.

The remainder of this chapter is organized as follows: In Sect. 5.2, we discuss the manner in which we can observe the chiral near field in the vicinity of metallic chiral structures. In addition, we propose a scheme to measure the 3D NF-CD using the optical force that visualizes CD with nm resolution by numerically demonstrating the CD map of the observed force on the gammadion metallic structures. In Sect. 5.3, we demonstrate that the NPs can be mechanically rotated and manipulated using the designed chiral field by plasmonic structures [25]. In this demonstration, we specifically consider that utilizing the nonlinear optical response considerably enhances the degree of freedom to manipulate NPs.

## 5.2 3D Near-Field CD by Optical-Force Measurement

One of the goals of analytical chemistry is to determine the structures of isolated single molecules. Accordingly, the single-molecule chiral analysis gains importance. To that end, the superchiral field is a promising tool [14–17], and its electromagnetic-field analysis is essential. However, in the aforementioned studies, the far-field CD (FF-CD) was evaluated based on the extinction of the light propagating through the target. The FF-CD signal is a convenient indicator that provides macroscopic information on the integrated target ensemble. However, nanoscale structures such as single molecules are averaged together with the information of the microscopic

surrounding environment. Therefore, to maximize the potential of superchiral fields for measuring single molecules, we must develop a measuring device for the in-situ evaluation of the near field.

Recent studies reported the NF-CDs for various nanostructures and obtained characteristic signals that reflected their local geometry [10–13]. However, these studies measured the 2D projections of the NF-CD, which are the images of the propagated component of the scattered light in the vicinity of the target. Therefore, it is difficult to obtain the information regarding the localized longitudinal field, which is a significant component of the near field. Hence, we propose another scheme that uses optical force under laser illumination. If the targeted sample and the probe tip of the atomic force microscope are irradiated by light, dipole-dipole interaction occurs between them, and the near-field profile around the sample can be obtained by detecting the induced force, which is proportional to the gradient of the field intensity. This technique is called photoinduced force microscopy (PiFM) [26]. Because this scheme is sensitive to the longitudinal component of the polarization of the chiral near field, it can simultaneously acquire the 3D profile of the near field, i.e., the transverse and localized longitudinal components. To examine the validity of the scheme, for the superchiral field near the specific metallic structure, the force-measurement calculation results are compared with the electromagnetic-field calculation results.

### 5.2.1 Model and Method

The system under consideration is depicted in Fig. 5.1. In our numerical demonstration, the metallic structure, which comprises four gold gammadions, is set on the dielectric substrate. This structure exhibits large FF-CD [4] and boosts the FF-CD of a few molecules [14, 15]. The tip probe is modeled using a gold hemisphere and is scanned at 5 nm above the metallic structure. The circularly polarized plane wave lights are illuminated from below the substrate and propagate along the  $z$ -axis. We calculated the total electric field near the metallic gammadion and probe tip to detect the optical force.

Based on linear response theory, we can express the induced polarization  $\mathbf{P}(\mathbf{r}_i, \omega) = \chi(\mathbf{r}_i, \omega)\mathbf{E}(\mathbf{r}_i, \omega)$  at the position  $\mathbf{r}_i$ , i.e., the  $i$ -th cubic cell of the volume  $V_c$ , where  $\mathbf{E}(\mathbf{r}_i, \omega)$  denotes the total electric field. We set the local susceptibility in the substrate to  $\chi(\mathbf{r}, \omega) = \epsilon_s - 1$  with the relative permittivity set as  $\epsilon_s = 2.25$ . On the other hand, the gold gammadion structures and the probe tip are composed of cells, whose dielectric constant is represented using the Drude model [27]. The dielectric function here is Drude-type, i.e.,

$$\chi_{\text{metal}}(\omega) = \epsilon_{\text{metal}}(\omega) - 1 = \epsilon_b - 1 - \frac{(\hbar\Omega^{\text{pl}})^2}{\hbar^2\omega^2 + i\hbar\omega(\hbar\Gamma^{\text{bulk}} + \frac{\hbar\nu_{\text{F}}}{L_{\text{eff}})}}, \quad (5.1)$$

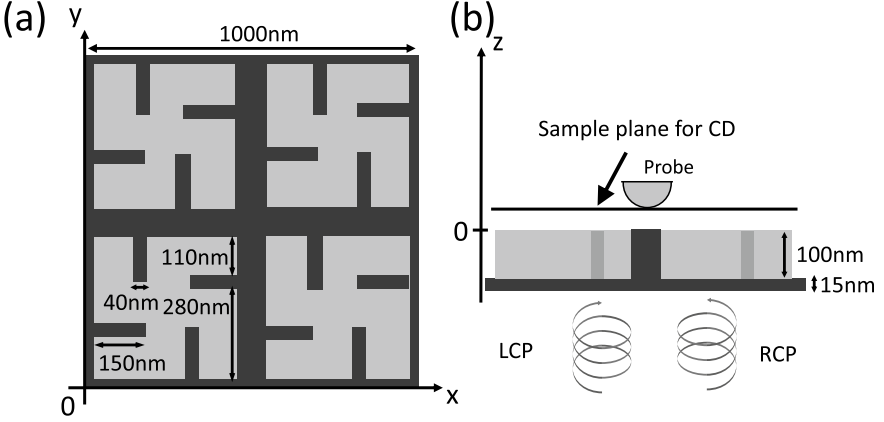


**Fig. 5.1** Incident light condition and metallic structure on the dielectric substrate. The incident light is a circularly polarized plane wave and propagates along the  $z$ -axis. We allocate a calculation space of  $1000 \times 1000 \times 250 \text{ nm}^3$  and discretize the space using cubes of the volume  $V_c 5 \times 5 \times 5 \text{ nm}^3$ . The CD signal is the summation of the field intensity of the sample surface. The top view (a) and side view (b) of the gammadion structure on the substrate. The length of each gammadion arm is illustrated, and the thickness is 100 nm. The relative permittivity and thickness of the substrate are set to 2.25 and 15 nm, respectively. The gammadion structure is aligned at the intervals of 500 nm. The scanning probe illustrated in (b) is a gold hemisphere of radius 50 nm. The size of the center gap is  $75 \times 75 \text{ nm}^2$ . The scanning area is  $90 \times 90 \text{ nm}^2$

where  $\epsilon_b$  denotes the background dielectric constant of the metal,  $\Omega^{\text{pl}}$  the bulk plasma frequency,  $\Gamma^{\text{bulk}}$  the electron-relaxation constant of the metal,  $V_f$  the Fermi velocity, and  $L_{\text{eff}}$  the effective mean free path of the electrons. We have used the following parameters for the gold cells:  $\epsilon_b = 12.0$ ,  $\hbar\Omega^{\text{pl}} = 8.958 \text{ eV}$ ,  $\hbar\Gamma^{\text{bulk}} = 72.3 \text{ meV}$ ,  $\hbar v_f = 0.9215 \text{ eV}\cdot\text{nm}$ , and  $L_{\text{eff}} = 20 \text{ nm}$  [27]. In the calculations, we have used the discrete dipole approximation (DDA) method [28] to solve Maxwell's equation. We solved the following discretized integral equation:

$$\mathbf{E}(\mathbf{r}_i, \omega) = \mathbf{E}_0(\mathbf{r}_i, \omega) + \sum_j \mathbf{G}_0(\mathbf{r}_i, \mathbf{r}_j, \omega) \mathbf{P}_{\text{metal}}(\mathbf{r}_j, \omega) V_c, \quad (5.2)$$

where  $\mathbf{E}_0$  is the electric field of the incident light, and  $\mathbf{G}_0$  the Green's function of the electric field vector in vacuum. In the preceding equation, we take the sum for all the cells including the dielectric substrate, gammadion structures, and probe tip. Therefore, the calculated response field takes into account the nonlocal response, and the influence of the shape of the metals.

Notably, the definition of the circularly polarized light is not clear in case of electric fields that contain much localized components. To evaluate the circularly polarized components along the  $z$ -,  $y$ - and  $x$ -directions, the following projections were employed:

$$E_{xy^\mp}(\mathbf{r}_i, \omega) = \frac{1}{\sqrt{2}}(1, \pm i, 0)\mathbf{E}(\mathbf{r}_i, \omega), \quad (5.3)$$

$$E_{xz^\mp}(\mathbf{r}_i, \omega) = \frac{1}{\sqrt{2}}(1, 0, \pm i)\mathbf{E}(\mathbf{r}_i, \omega), \quad (5.4)$$

$$E_{yz^\mp}(\mathbf{r}_i, \omega) = \frac{1}{\sqrt{2}}(0, \pm i, 1)\mathbf{E}(\mathbf{r}_i, \omega). \quad (5.5)$$

The “-” and “+” signs denote the left-handed circularly polarized (LCP) component and right-handed circularly polarized (RCP) component, respectively, of the electric field. In Fig. 5.2, we have mapped each electric-field polarization component directed along each direction just above the metallic structures (i.e., at  $z = 5$  nm). Here, the incident light is the RCP light, and the electric-field intensity is normalized using the incident-light intensity  $|E_0|^2$ . The LCP component of the near field in the  $xy$ -plane is small at the center gap of the gammadion metallic structure, while the RCP component is remarkably enhanced there (see Fig. 5.2 a, b). In Fig. 5.2 c, d, we show the circularly polarized components in the  $xz$ -plane; these components include the longitudinal component of the near field. Compared with the case in the  $xy$ -plane, the longitudinal component appears more locally at the edges of the metallic structures. In the  $yz$ -plane, similar maps are obtained (no figure). Notably, a considerable part of the electric field is occupied by the longitudinal near-field component, and the polarizations do not change with propagation unlike those in the case of the circularly polarized plane wave. This implies that the longitudinal component of the near field in NF-CD must be a significant component of the superchiral field.

The proposed measurement scheme uses the time-averaged optical force on the scanning probe tip, as depicted in Fig. 5.1 b. We derive the optical force on the probe tip as follows [29]:

$$\langle \mathbf{F}(\omega) \rangle = \frac{1}{2} \text{Re} \left[ \int_{V_{\text{tip}}} d\mathbf{r} [\nabla \mathbf{E}(\mathbf{r}, \omega)^*] \cdot \mathbf{P}_{\text{probe}}(\mathbf{r}, \omega) \right] = \mathbf{F}_z(\omega) + \mathbf{F}_{xy}(\omega), \quad (5.6)$$

where the integration range is within the volume of the probe tip  $V_{\text{tip}}$ . In the present setup, a strong and steep localized field gradient appears between the tip and the metal. Thus, the gradient force is dominant in the optical force, where the vertical force  $F_z(\omega)$  is proportional to the gradient in the  $z$ -direction of the probe-target potential  $U(\mathbf{r})$ , and proportional to  $|\mathbf{E}(\mathbf{r}, \omega)|^2$ . In addition, the lateral photo-induced force  $\mathbf{F}_{xy}$  is approximated by the differentiation of  $U(\mathbf{r})$  in the lateral  $xy$ -plane [30]. Here, the electric field  $\mathbf{E}(\mathbf{r}, \omega)$  includes the field scattered by the gold probe tip, and it considerably differs from the one that is observed when only the metallic structures are set. The numerical simulations presented in the following subsections show that the optical force well reproduces the CD of the superchiral field near the metal structure, despite the change in the electric field profile with and without the probe tip.

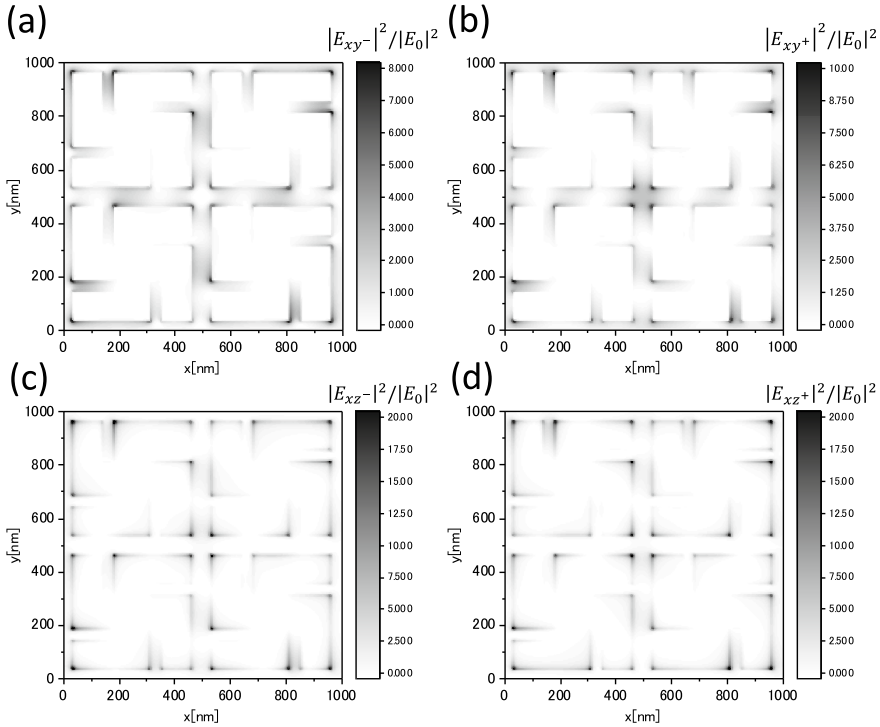


**Fig. 5.2** Circularly polarized components are mapped along each direction at 5 nm above the top plane of the metallic structure. As the incident field, the RCP light at 1.65 eV is employed. **a, b** The intensity map of the LCP component **(a)** and RCP component **(b)** in the  $xy$ -plane. **c, d** The intensity map of the LCP component **(c)** and RCP component **(d)** in the  $xz$ -plane. The color bars indicate the intensity of each circularly polarized component normalized using the incident-light intensity

## 5.2.2 CD Spectra and NF-CD Maps

Prior to calculating the optical force, we analyzed the CD of the electric field to be referenced. We allocated a computational space of  $1000 \times 1000 \times 1125 \text{ nm}^3$  and discretized it into the cubes of  $5 \times 5 \times 5 \text{ nm}^3$ . Since the localized field is considerably attenuated at  $z \sim 1000 \text{ nm}$ , the influence of the boundary of the computational space on the superchiral field is negligibly small. Throughout this work, we defined the NF-CD signal as  $\Delta T = T_{\text{RCP}} - T_{\text{LCP}}$ , where  $T_{\text{RCP}}$  and  $T_{\text{LCP}}$  denote the transmitted field intensities of the RCP and LCP optical signals, respectively. This is because we considered the in-situ CD of the superchiral field, and could not evaluate the CD from the difference in the extinction far from the metal structures.

As illustrated in Fig. 5.3 a, b, we investigated the CD spectra both at 5 and 1000 nm above the top plane of the metallic structure, respectively. We have plotted  $\overline{\Delta T}$ , which is the average of  $\Delta T$  in each  $z$  over an area of  $1000 \times 1000 \text{ nm}^2$ . To better examine the effect of the longitudinal field on the CD, we decomposed the CD into

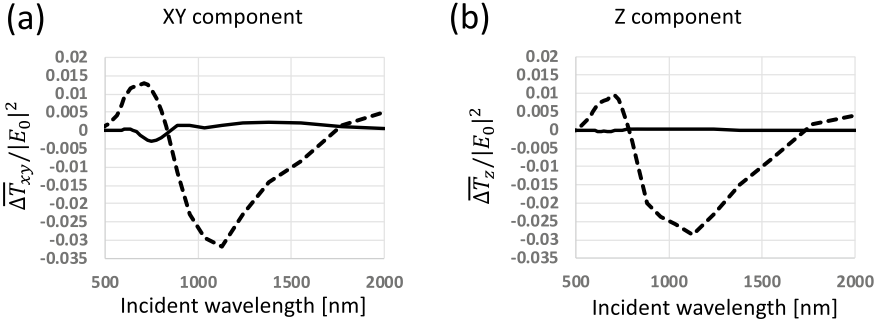


**Fig. 5.3** CD spectra of the **a**  $xy$  component and **b**  $z$  component. The CD spectra at 5 nm (broken line) and 1000 nm (solid line) above the top plane of the metallic structure

the in-plane component (normal to the incident propagation)  $\Delta T_{xy}$  and  $z$  component  $\Delta T_z$ , and both are compared with each other. Here,  $\Delta T_i$  denotes the intensity of the  $i$ -component of the transmitted light, and  $\Delta T_{xy} = \Delta T_x + \Delta T_y$ . At a considerably distant region above the metal (i.e.,  $z = 1000$  nm), the intensity of the longitudinal  $z$ -component becomes approximately 10 times smaller than that of the in-plane one. In the conventional FF-CD measurement, the distance between the probe and sample is more than 1 mm; hence, the longitudinal component can be safely neglected. However, at  $z = 5$  nm above the sample, the longitudinal CD intensity is of the same order of magnitude as the in-plane one. Moreover, even for the in-plane component, the NF-CD spectra ( $z = 5$  nm) are fairly different from the those at  $z = 1000$  nm. This clearly indicates that we cannot estimate the NF-CD spectra from the FF-CD ones, as confirmed by the experiment [13].

In Fig. 5.4a–d, we present the NF-CD contour maps of the transmitted in-plane intensity  $\Delta T_{xy}$  and the vertical longitudinal one  $\Delta T_z$  at  $z = 5$  nm. The incident RCP light has the energy of 1.65 eV (wavelength of approximately  $\lambda = 750$  nm), where we observe the CD peak in Fig. 5.3. Because half of the wavelength is as long as each gammadion, the NF-CD maps should reflect well the geometrical figure of the system. Notably, the in-plane NF-CD distributes differently than the longitudinal one. The in-plane components of the NF-CD appear mainly in the gap between the metallic structures, while the longitudinal components are concentrated on the gammadion edges. Therefore, while examining the spatial structure of the NF-CD, it is difficult to estimate the structure of its longitudinal component by using the structure of the in-plane component.

### 5.2.3 CD of Optical Force

As can be seen in the previous subsection, observing the 3D figure, as well as the longitudinal component of the superchiral field, for individual metallic structures



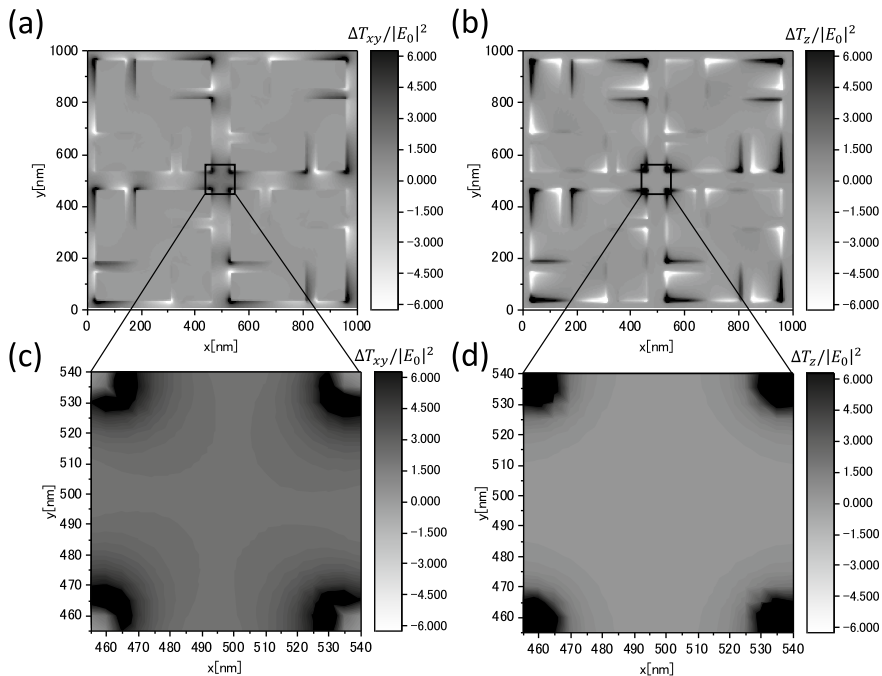


**Fig. 5.4** NF-CD maps about the  $xy$ - and  $z$ -components on sample planes. **a, b** NF-CD maps about the  $xy$ - and  $z$ -component at  $z = 5$  nm. The grayscale bar indicates the CD intensity normalized using the incident-light intensity. **c, d** Enlarged view near the center gap of the metallic structure in **(a, b)**. The grayscale bar indicates the CD intensity normalized using the incident-light intensity  $|E_0|^2$

is fairly important. We simulated the 3D NF-CD measurement by calculating the time-averaged optical force that acts on the metallic probe tip [29, 31]. Using a state-of-the-art technique of PiFM, the spatial resolution of 1 nm was achieved [32]. In addition, the technique enables 3D vector force imaging [30].

When the probe tip is scanned on the gap area of the four gammadians in Fig. 5.1 a at  $z = 5$  nm, we calculated the difference between the optical forces when illuminated with the LCP and RCP lights. We set the incident light intensity to  $1 \text{ kW/cm}^2$  and the energy is the same as that in the previous subsection. The computational space is  $1000 \times 1000 \times 250 \text{ nm}^3$ , which is smaller in the  $z$ -direction compared to the space defined in the previous subsection. Since the localized field between the probe tip and metal structure is the dominant contributor to the photo-induced force, we can ignore the influence due to the space boundary. The difference of the  $z$ -component of the optical force is plotted in Fig. 5.5 a. The gradients along the  $z$ -direction of  $\Delta T_{xy}$  and  $\Delta T_z$  are depicted in Fig. 5.5 b, c. If the vertical force  $F_z(\mathbf{r})$  on the probe is integrated over  $z$ , we can obtain the field intensity and the probe-target potential  $U(\mathbf{r})$ . Instead of performing the aforementioned integration, we have depicted the

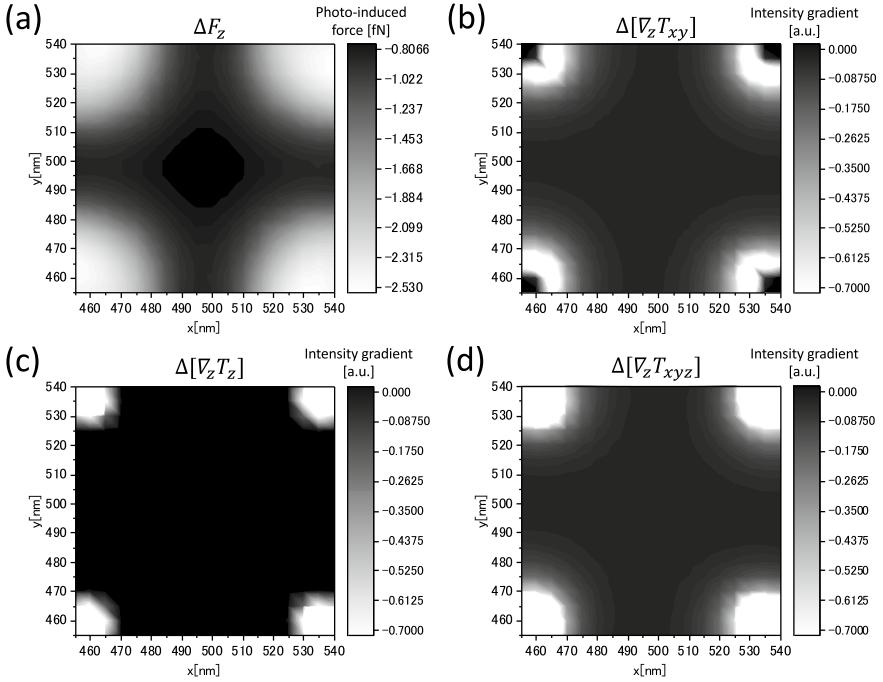


**Fig. 5.5** **a** Contour map of the difference between the z-directed photo-induced forces on the probe under the RCP illumination and those under the LCP illumination. **b–d** The differentiations in the vertical direction  $\nabla_z$  of the in-plane CD, longitudinal CD and their summation are mapped

gradient of the field intensities in Fig. 5.5 b, c and compared them with the forces depicted in Fig. 5.5 a.

Notably, the map in Fig. 5.5 a resembles that in Fig. 5.5 b inside the gap area, as the longitudinal component is weak in this region. However, at the corner regions, the gradient of the longitudinal component becomes remarkably large, as depicted in Fig. 5.5 c. This situation is well reflected in the corner regions in Fig. 5.5 a. Specifically, the field gradient at the corner regions is weak for the xy-component, as depicted in Fig. 5.5 b, whereas the induced force at the corner regions becomes strong, as depicted in Fig. 5.5 a. This situation becomes clearer if we note that the map of the gradient of sum  $\Delta T_{xyz} = \Delta T_{xy} + \Delta T_z$  shown in Fig. 5.5 d is very similar to the map in Fig. 5.5 a. Therefore, the force map successfully provides information including the contribution of the longitudinal component that cannot be observed using the aperture-type scanning near-field optical microscope.

Finally, the feasibility of this proposal warrants a mention. The sensitivity of the optical force enables the application of the present scheme in the state-of-the-art technology of optical-force microscope with reasonable incident intensity [32]. However, the question may arise whether the probe tip might change the image from the actual field strength profile in our proposal. In practice, the force map blurs slightly, as the

probe-tip diameter, i.e., 100 nm, is greater than the gap spacing between the gammadions in Fig. 5.5 b, c. However, when the spacing between the gammadions and probe tip is small, the electric-field enhancement is determined only by the structure near the probe tip. Therefore, the difference between the profile of the electric field and the one measured using the force is not significant. In actual experiments using optical-force microscope, the tip-sample spacing is less than 1 nm. Therefore, we can obtain satisfactory correspondence between the optical force and field gradients in actual experiments, as well as obtain further enhanced optical force. The information obtained provides significant insight into the spatial structures of the 3D NF-CD. For the cases in the presence of targeted molecules on the metallic structures, more detailed analyses of the force map to obtain the 3D NF-CD information are desired.

### 5.3 Optical Force to Rotate Nano-Particles in Nanoscale Area

According to Maxwell's theory of electromagnetism, both traveling and standing light waves can exert mechanical force on targets because of scattering and absorption. This force is sometimes called the "optical force". The optical force is classified as a dissipative force, which arises from the transfer of optical momentum to a substance by absorption and scattering, and a gradient force due to the electromagnetic interaction between the induced polarization and the incident light. The dissipative force usually pushes and transports particles, and the gradient force can be used to attract and trap particles. One of the most impressive applications of this force is an optical tweezer with a focused laser, as proposed by Ashkin et al. [33]. This optical force is attributed to the transfer of momentum from light to the matter target. Similarly, the spin and orbital angular momenta of light also can be transferred to the mechanical motion of small particles. The light with orbital angular momentum, such as a Laguerre–Gaussian (LG) beam [34], is considered to result in the orbital rotation of targets. Notably, micro-particles are swirled along a ring-shaped region, where the field intensity of the LG beam is strong [35]. However, presently, it is not known how the optical manipulation for the rotational control in a nanoscale area can be performed.

This section is devoted to discussing the chiral interaction between light and metallic nanocomplexes, wherein the chiral interaction induces rotational motion of nano-particles (NPs) in a nanoscale region. In recent years, the target of optical manipulation has shifted to the nanometer-scale. However, within the Rayleigh scattering regime, the optical force is approximately proportional to the volume of the object, hence, the induced force is quite weak. To enhance the force to overcome the disturbance due to the environment of NPs, the use of the evanescent field with a steep gradient of the electric field has been proposed [36, 37], and recently, the trapping of NPs associated with LSP resonance has been extensively studied [38–44]. Another approach is the use of resonance with transitions between the electronic levels in

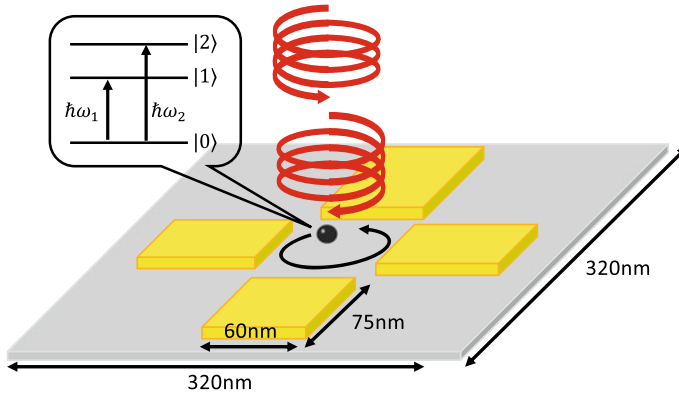


**Fig. 5.6** System setup. The image of super-resolution rotational optical manipulation inside the tetramer metallic structures with a circularly polarized plane wave. The nanostructures are assumed to be four gold panels that form nanogaps on the glass substrate. The size of each panel is  $75 \times 60 \times 20 \text{ nm}^3$ , and the gaps are  $\sqrt{10^2 + 10^2} \simeq 14 \text{ nm}$ . The NP is assumed to have three levels as depicted in the inset. The size of the NP is set to be  $5 \times 5 \times 5 \text{ nm}^3$ . (The entire system is divided into cells of size  $5 \times 5 \times 5 \text{ nm}^3$  for the DDA calculation.) In both the cases, the incident lights propagate along the negative  $z$ -axis. See, [25]

NPs [31, 45–49]. In general, nanostructures have quantized electronic levels. Thus, the optical force can be resonantly enhanced if the frequency of the incident light coincides with their transition energies. Successful trapping and transport of NPs using resonant laser light have been previously reported [50–54]. Herein, we have demonstrated a scheme to realize rotation and the switching direction of NPs in a nanoscale region using metallic nanocomplexes with LSP resonance and the resonant optical response of NPs [25]. In particular, optical nonlinearity is key to realizing the rotational motion of NPs. Using the resonant optical response often results in optical nonlinearities, thereby enhancing both the trapping efficiency and the degree of freedom of NP manipulation [49, 55, 56]. We have shown that by introducing the optical nonlinearity of NPs due to LSP resonance, nanoscale NP rotation, and the switching of the direction is possible. The transfer of the orbital angular momentum of light to a small object has potential applications in various technologies such as nanoelectromechanical systems and chiral sensing [57, 58].

### 5.3.1 Model and Method

We assumed a metallic nanocomplex as a platform for rotating the NP within the nanoscale region, as illustrated in Fig. 5.6. When it is irradiated using a circularly polarized light with the spin angular momentum of  $s = \pm 1$ , a nano-optical vortex, which is connected to the LSPs near the metal, is generated. Recent theoretical works revealed that the excited plasmon modes inside the gap of the metallic nanocomplex

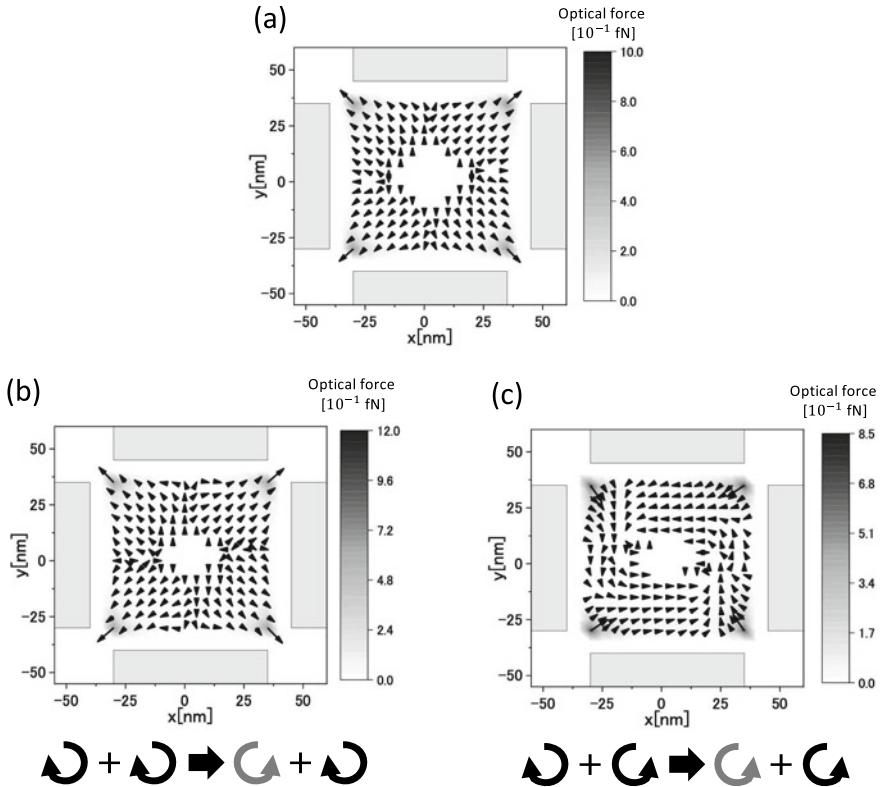


**Fig. 5.7** Optical-force map inside the metallic nanocomplex. The black arrows indicate the force vectors in the x-y plane. The grayscale bars represent the magnitude of the optical force. The manipulation light and pump light energies are resonant to the 0–1 and 0–2 transitions, respectively. **a** The case that contains only the RCP manipulation light with the spin angular momentum of  $s = +1$ . The intensity is  $100 \text{ kW/cm}^2$ . **b** The case that contains both the RCP pump light and RCP manipulation light with the intensities of  $100 \text{ kW/cm}^2$ . **c** The case that contains both the LCP pump light and RCP manipulation light with the intensities of  $100 \text{ kW/cm}^2$ . In this case, the manipulation light energy is slightly red-detuned ( $1.798 \text{ eV}$ ). The arrows that draw circle below **b**, **c** show the rotation direction of the radiation force due to the pump light and manipulation light, respectively. (Reprinted with permission from [25] ©The Optical Society.)

can be determined using the symmetry of the metallic structures and orbital angular momentum of the incident light [18]. Notably, we employed the tetramer structure because of its satisfactory matching with the modeling in the DDA method [28].

To calculate the optical force that acts on the NP, we considered two features. One is to assume a specific metal structure using the DDA method, as done in the previous section. The other is to assume a three-level NP with levels  $\{0, 1, 2\}$  as depicted in Fig. 5.6 and to incorporate the nonlinear optical response there. Further, we ignored the nonlinear effect and temperature dependence of the dielectric constant in the metal. This is because the effects of possible saturation or broadening do not

change the nature of the results of the intensity regions considered, and only slight quantitative corrections are expected [59, 60].

The expression of the time-averaged optical force is the same as (5.6), where  $\mathbf{P}_{\text{probe}}(\mathbf{r}, \omega)$  should be replaced by  $\mathbf{P}_{\text{NP}}(\mathbf{r}, \omega)$ , which denotes the induced polarization of the NP. The integration was performed over the volume of the NP. We calculated the electric field  $\mathbf{E}$  and polarization  $\mathbf{P}_{\text{NP}}$  according to the following process. We obtained the simultaneous master equations of the three-level NP and Maxwell's equations. To solve the Maxwell's equations, we solved the same equation as (5.2) with (5.1) by using the same parameters of gold used in the previous section. The formal solution of the total electric field in the presence of the NP is expressed as the following integral equation:

$$\mathbf{E}(\mathbf{r}_i, \omega) = \mathbf{E}_b(\mathbf{r}_i, \omega) + \sum_j^{\text{NP}} \mathbf{G}(\mathbf{r}_i, \mathbf{r}_j, \omega) \mathbf{P}_{\text{NP}}(\mathbf{r}_j, \omega) V_j, \quad (5.7)$$

where  $\mathbf{G}$  denotes the renormalized Green's function that includes the geometrical information of the metallic structures. To derive the renormalized Green's function of arbitrary-shaped metallic structures, we solved the following integral equation:

$$\mathbf{G}(\mathbf{r}_i, \mathbf{r}_j, \omega) = \mathbf{G}_0(\mathbf{r}_i, \mathbf{r}_j, \omega) + \sum_k^{\text{metal}} \mathbf{G}_0(\mathbf{r}_i, \mathbf{r}_k, \omega) \chi_{\text{metal}}(\omega) \mathbf{G}(\mathbf{r}_k, \mathbf{r}_j, \omega) V_k, \quad (5.8)$$

where  $\mathbf{G}_0$  denotes the free-space Green's function.

The NP polarization should be determined using the total electric field. Accordingly, we assumed the following Hamiltonian of NP with isotropic dipole moments:

$$\hat{H}(t) = \sum_{a=1,2} \hbar\omega_a \hat{\sigma}_{aa} - \int_V d\mathbf{r} \hat{P}_{\text{NP}}(\mathbf{r}) |\mathbf{E}(\mathbf{r}, t)|, \quad (5.9)$$

where index  $a$  represents the excited levels of the NP,  $\hbar\omega_a$  the transition energy between the ground state 0 and state  $a$  of the NP, and  $\hat{\sigma}_{aa}$  the population of state  $a$ . Further, we described the induced polarization as follows:

$$\hat{P}_{\text{NP}}(\mathbf{r}) = \sum_{k<l} d_{kl} \hat{\sigma}_{kl} \delta(\mathbf{r} - \mathbf{r}_p) + \text{h.c.}, \quad (5.10)$$

where  $d_{kl}$  denotes the matrix element of the dipole moment. In addition,  $\hat{\sigma}$  denotes the dimensionless polarization operator,  $\mathbf{r}_p$  its position, and indices  $k = \{0, 1\}$  and  $l = \{1, 2\}$  its energy levels. The Markovian master equation for the three-level NP is described using the following equation [61]:

$$\begin{aligned} \frac{d}{dt}\rho(t) = & -\frac{i}{\hbar}[\hat{H}(t), \rho(t)] + \sum_{k<l} \frac{\gamma_{kl}}{2} [2\hat{\sigma}_{kl}\rho(t)\hat{\sigma}_{lk} - \{\hat{\sigma}_{lk}\hat{\sigma}_{kl}, \rho(t)\}] \\ & + \sum_{(l\neq m)} \frac{\gamma_{pl}}{2} [(\hat{\sigma}_{ll} - \hat{\sigma}_{mm} - \hat{\sigma}_{00})\rho(t)(\hat{\sigma}_{ll} - \hat{\sigma}_{mm} - \hat{\sigma}_{00}) - \rho(t)], \end{aligned} \quad (5.11)$$

where  $\rho$  denotes the density matrix of the NP and  $\gamma$  ( $\gamma_p$ ) a nonradiative population damping constant (pure dephasing constant). Notably, the radiative decay rate of the NP is automatically incorporated into the calculation by using the renormalized Green's function. Using (5.11), we derived the equations of motion for the polarization operator  $\langle\sigma_{kl}\rangle$ , and expanded via the Fourier components with respect to the incident frequencies.

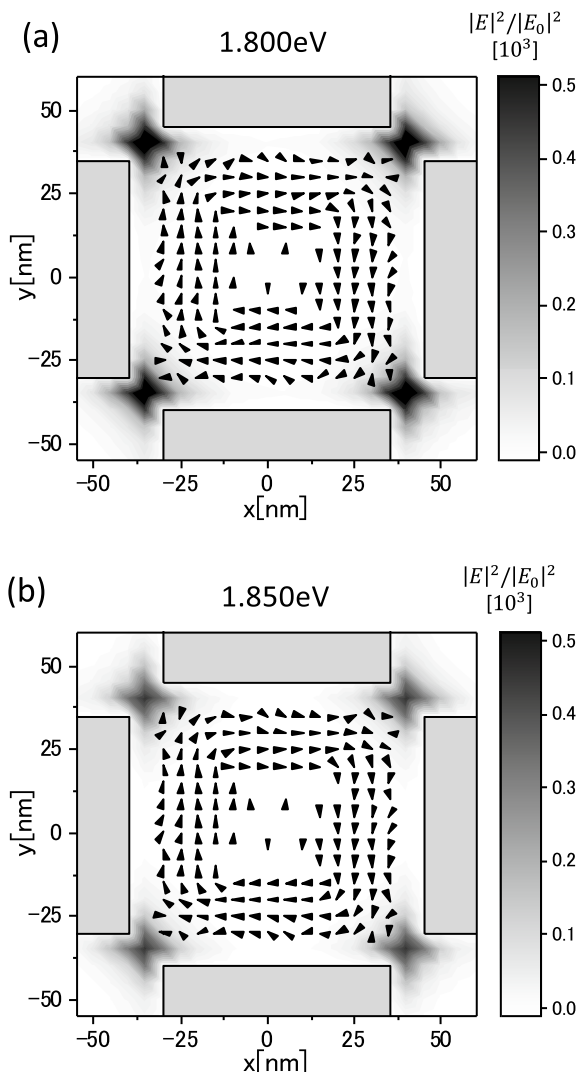
Using the mean-field approximation, we solved  $\langle\sigma_{kl}\rangle$  and  $\mathbf{E}(\mathbf{r}_i, \omega)$  in a self-consistent manner; thus, we obtained the NP polarization and total electric field. In the calculation, the Green's function was expanded into the Fourier components, as well as the polarization, and we considered only the frequency components near the plasmon resonance. In addition, we assumed that the directions of the dipole moments of the NP coincide with those of the background electric-field resonant to each transition. In this solution, if we consider up to the higher-order correlations in the master equation, we can take into account the effects of the nonlinear optical response in the NP beyond the perturbation regime, so that the population inversion can be treated. Substituting the obtained  $\mathbf{E}$  and  $\mathbf{P}$  in (5.6), we obtained the optical force, as well as the nonlinear effect of the NP.

### 5.3.2 Optical Force to Rotate the NP

In the numerical simulation, we employed the parameters by considering fluorescent dyes; the resonance energies for the 0–1 and 0–2 transitions were 1.80 and 1.85 eV, respectively. The dipole moments of the NP were set to 10 Debye for the 1–0 and 2–0 transitions, and this is realistic for the molecular aggregate of size  $5^3 \text{ nm}^3$ . The nonradiative population decay constants for the 1–0 and 2–1 transitions were set to  $1 \mu\text{eV}$  and  $20 \text{ meV}$ , respectively. The pure dephasing constant for the excited levels was  $2 \text{ meV}$ . As for the incident lasers, we considered two plane waves with circular polarization, and these waves were irradiated from above. The incident waves, hereinafter referred to as manipulation light and pump light, had spin angular momentum  $s = \pm 1$  and energies resonant to the 0–1 and 0–2 transitions, respectively. The rotation direction of the NP depends on its spin angular momentum. Notably, the spin angular momentum of light can result in the orbital motion of the NP by utilizing the metallic nanocomplex.

In Fig. 5.7a, we depict the force map inside the tetramer structure in the x-y plane, where only the RCP manipulation light is irradiated with the spin angular momentum  $s = +1$ , and the intensity is  $100 \text{ kW/cm}^2$ . In this case, the dissipative force to rotate the NP saturates because of the nonlinearity, and the gradient force becomes the

**Fig. 5.8** Optical current map inside the metallic nanocomplex. The black arrows denote the optical current vectors. The grayscale bars show the field intensity. **a** Incident energy is 1.80 eV, and the spin angular momentum is  $s = +1$ . **b** Incident energy is 1.85 eV, and the spin angular momentum is  $s = +1$ . (Reprinted with permission from [25] ©The Optical Society.)



dominant force to move the NP. Therefore, the rotational force is suppressed, and the NP is attracted toward the gaps where the field intensity is strong. However, when the pump light is switched on, the pump intensity enables us to adjust the ratio of the dissipative force to gradient force. The criterion to adjust this ratio by using nonlinearity is explained in Appendix 1.

In Fig. 5.7b, we depict a force map, in which the pump light has the same spin angular momentum and intensity as those of the manipulation light. In this case, the 0–2 transition by the strong LSP field easily makes the population of the 1 state exceed 0.5; i.e., population inversion occurs. This inversion reverses the force vector



induced by the manipulation light [49]. Consequently, although both the incident lights have the same spin angular momentum, the rotation direction of the manipulation light becomes opposite to that of the pump light. Therefore, their rotational forces (dissipative forces) eliminate each other and, hence, the optical force to rotate the NP is not induced, although the spin directions of both the lights are parallel. Subsequently, we examined the case in which the LCP pump light has different spin angular momenta. In this case, the rotational forces reinforce each other. Therefore, the rotational force of the NP was realized as depicted in Fig. 5.7c. Notably, we can avoid pointing the optical force outward by slightly red-detuning the manipulation-light energy to the resonance of the 0–1 transition (see Appendix 2). This rotational force is sufficiently strong because of the LSP. Therefore, one can realize the rotational manipulation at the nanometer scale and can selectively control the rotational direction by switching the pump light.

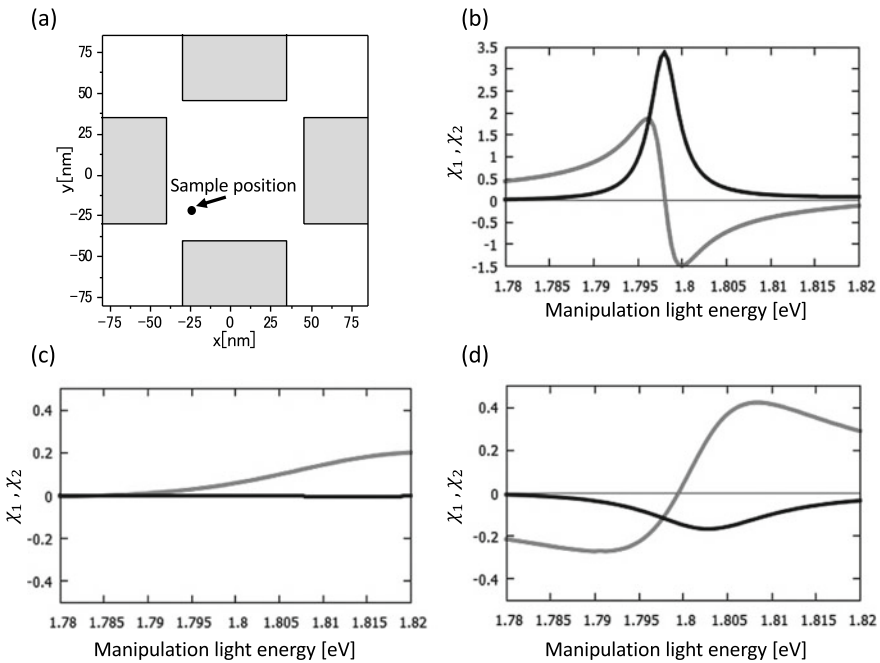


**Fig. 5.9** **a** Sample position of the NP inside the tetramer structure in calculating susceptibility  $\chi_{1(2)}$ , which is induced by the manipulation light. The coordinates of the position are set to be  $(x, y, z) = (-20 \text{ nm}, -20 \text{ nm}, 25 \text{ nm})$ . **b–d** Spectra of susceptibility  $\chi_1$  (gray line) and  $\chi_2$  (black line) as the functions of the manipulation light energy. **b** Case with weak excitation. The intensity of the manipulation light is  $1 \text{ W/cm}^2$ . **c** Case with strong excitation. The intensity of the manipulation light is  $100 \text{ kW/cm}^2$ . **d** Case with stimulated emission. The pump light energy and intensity are  $1.85 \text{ eV}$  and  $100 \text{ kW/cm}^2$ , respectively. The intensity of the manipulation light is  $100 \text{ kW/cm}^2$ . (Reprinted with permission from [25] ©The Optical Society.)

### 5.3.3 Optical Current

To gain a better understanding of the optical force that rotates the NP inside the metallic nanocomplex, we considered the x-y component of the Poynting vector, which is zero for plane wave light. This vector, which is also referred to as optical current, contributes to the dissipative force exerted on the NP [62, 63]. The optical current is classified into orbital and spin parts [63]. In Fig. 5.8 a, b, we depict the orbital part of the time-averaged optical current inside the metallic nanocomplex when the circularly polarized light with  $s = +1$  is irradiated. Whether irradiating only the manipulation light (resonant to the 0–1 transition) or only the pump light (resonant to the 0–2 transition), the optical current flows clockwise inside the metallic nanocomplex. These results are consistent with the rotational force discussed in Fig. 5.7c, and also with the relation between population inversion and the rotational direction of the NP. In addition, it is observed that the direction of the rotational flow in the metallic nanocomplex depends on the direction of the optical current at the four gap positions. If the manipulation scheme suggested here is realized, the basic elements of manipulating the NP (pushing, pulling, and rotating) are also achieved. This will introduce new technologies not only for nanofabrication but also for nano-optomechanics that involve chiral materials and highly sensitive and selective chiral sensing.

## 5.4 Summary

Light–nanomatter chiral interaction has been a central subject of research in various domains for a long time. The development of nanofabrication technologies and single-molecular detection techniques take the study of this domain to a new stage. Particularly, the chiral interaction between light and metallic nanostructures has garnered attention because of its wide potential applications. Further, this phenomenon is the basis of our understanding of the nonlocal optical response, which is beyond the conventional model based on LWA or DA. For example, a strong CD of the localized field appears due to the geometric effect of the entire structure of the samples. The conversion of the spin angular momentum of light to orbital angular momentum via multipole excitation of nanoscale metallic complexes is also a peculiar manifestation of nonlocality.

One of the interesting aspects of optical response is the fact that its manifestation appears not only as optical signals but also as mechanical force induced on matter systems. Accordingly, in this chapter, we discussed the chiral interaction between light and metallic structures visualized and appearing in optical-force effects.

The first topic is the manner in which we can visualize the 3D NF-CD that appears in the vicinity of chiral metallic structures. The aperture-type scanning near-field optical microscope is a powerful tool to unveil the chiral near field. However, it is difficult to elucidate the 3D structure of superchiral field, especially around the

edges of metallic structures, as the longitudinal localized component is dominant there. However, optical force is significantly sensitive to the spatial distribution of the field, which includes both the transverse traveling component and longitudinal localized one. This sensitivity feature can be utilized to observe the 3D field distribution by using a microscope. Our numerical simulations showed that the optical-force microscope satisfactorily visualized the 3D NF-CD.

The second topic is the rotational-motion control of NPs in the nanoscale area, and this control is realized using the chiral interaction between the circularly polarized light and metallic nanocomplex. We theoretically demonstrated that the conversion between the spin angular momentum and orbital angular momentum using the aforementioned interaction induced the rotational motion of NPs. Furthermore, it was shown that by performing the balance control between the dissipation force and gradient force via nonlinear optical responses, we could switch the rotation direction of NPs.

The studies introduced in this chapter confirmed the essential roles of optical-force effects to research the chiral interactions at the metallic nanostructures that sustain LSP. It is important for various kinds of technologies to analyze molecular substances and control the mechanical motion of nanostructures via chiral interactions. The present results might stimulate further study of microscopic chiral interactions in various research domains.

**Acknowledgements** The authors thank Y. Togawa, S. Hashiyada, H. Okamoto and K. Sasaki for their fruitful discussions. This work was supported in part by JSPS KAKENHI Grant Number JP16H06504 for Scientific Research on Innovative Areas “Nano-Material Optical-Manipulation”.

## Appendix 1

### Balance Between Dissipative Force and Gradient Force Under a Strong Near Field [25]

To understand the balance between the dissipative force and gradient force exerted on an NP under a strong near field, we considered the time-averaged optical force as follows:

$$\langle \mathbf{F}(\omega) \rangle = \frac{1}{2} \text{Re} \left[ \int_V d\mathbf{r} [\nabla \mathbf{E}(\mathbf{r}, \omega)^*] \cdot \mathbf{P}_{\text{NP}}(\mathbf{r}, \omega) \right]. \quad (5.12)$$

Here, we consider an evanescent field with a simple profile as follows:

$$\mathbf{E}(\mathbf{r}, \omega) = \mathbf{E}(x, y) e^{i(k_1 + ik_2)z}, \quad (5.13)$$

where  $k_1$  and  $k_2$  denote the wavenumber and extinction coefficients along the  $z$ -direction, respectively. The induced polarization is represented using complex susceptibility as follows:

$$\mathbf{P}_{\text{NP}}(\mathbf{r}, \omega) = (\chi_1 + i\chi_2)\mathbf{E}(\mathbf{r}, \omega) = (\chi_1 + i\chi_2)\mathbf{E}(x, y)e^{i(k_1+i k_2)z}. \quad (5.14)$$

The real (imaginary) part of NP's susceptibility is given by  $\chi_{1(2)}$ . Substituting (5.13) and (5.14) in (5.12) and regarding the induced polarization as the point dipole, the optical force is written as follows:

$$\langle \mathbf{F}(\omega) \rangle = \frac{1}{2} V_{\text{NP}} \left[ \frac{1}{2} \chi_1 \nabla_{x,y} |\mathbf{E}|^2 - \chi_1 k_2 |\mathbf{E}|^2 \mathbf{n}_z + \chi_2 k_1 |\mathbf{E}|^2 \mathbf{n}_z \right] e^{-2k_2 z}, \quad (5.15)$$

where  $V_{\text{NP}}$  denotes the volume of the NP,  $\nabla_{x,y}$  a 2D gradient, and  $\mathbf{n}_z$  a unit vector along the  $z$ -axis.

We classified the terms of (5.15) into dissipative and gradient forces. The first and third terms in the right hand side denote the conventional gradient force and dissipative force, respectively. In the presence of a finite  $k_2$ , we should also regard the second terms as the gradient force. Notably, under the LSP near-field, the gradient and dissipative forces depend on  $\chi_1$  and  $\chi_2$ , respectively. This means that one can control over the trapping/exclusion of the NP by adjusting the balance between  $\chi_1$  and  $\chi_2$  and by tuning the laser frequencies.

## Appendix 2

### Dissipative and Gradient Forces Induced by the Detuned Light [25]

When the non-resonant light is radiated,  $\chi_1$  and  $\chi_2$  are constant for light energy. However, the resonant polarization in the linear optical response results in dispersion-type  $\chi_1$  and Lorentz-type  $\chi_2$ . Therefore, their ratio drastically changes near the resonant energy of NP. Moreover, strong nonlinear optical effects such as absorption saturation and population inversion can result in the sign inversion of  $\chi_1$  and  $\chi_2$ . Here, we have regarded the ratio of  $\chi_1$  to  $\chi_2$  as that of gradient force to dissipative force, and demonstrated it for the following three cases: weak excitation, strong excitation, and stimulated emission.

In Fig. 5.9b–d, we depict the real and imaginary parts of the induced polarization of the NP at the sample position indicated in Fig. 5.9a. The polarization includes the resonant and non-resonant elements for the 0–1 and 0–2 transitions that are induced by the manipulation light. The parameter of the NP is the same as that in the main text. Under the weak excitation, the nonlinear optical effects are negligible, and the polarization obeys the linear optical response. Notably, the resonant energy (e.g., the peak energy of  $\chi_2$ ) is slightly red-shifted because of the metal-NP interaction. Under strong excitation,  $\chi_2$  is approximately zero, as the absorption and emission balance with each other owing to the absorption saturation. With respect to  $\chi_1$ , it becomes large as the manipulation light energy increases. This is because the absorption saturation effect suppresses the polarization with the 0–1 transition, and the polarization with the 0–2 transition starts to appear. In addition, in the presence of the pump light, the sign of the susceptibility is inverted, compared with the weakly excited case. The

negative value of  $\chi_2$  does not indicate reduction but gain. In other words, the negative value indicates the generation of the stimulated emission. The stimulated emission also results in the sign inversion of  $\chi_1$ . Inside the tetramer structure, the dissipative force induces orbital motion, and the gradient force points toward the hotspots at gap areas. In Fig. 5.7b, we have employed the red-detuned manipulation light and utilize the repulsive force (negative value of  $\chi_1$ ) from the hotspots, as depicted in Fig. 5.9d.

## References

1. Y. Tang, A.E. Cohen, *Phys. Rev. Lett.* **104**(16), 163901 (2010)
2. A. Papakostas, A. Potts, D. Bagnall, S. Prosvirnin, H. Coles, N. Zheludev, *Phys. Rev. Lett.* **90**(10), 107404 (2003)
3. T. Vallius, K. Jefimovs, J. Turunen, P. Vahimaa, Y. Svirko, *Appl. Phys. Lett.* **83**(2), 234 (2003)
4. M. Kuwata-Gonokami, N. Saito, Y. Ino, M. Kauranen, K. Jefimovs, T. Vallius, J. Turunen, Y. Svirko, *Phys. Rev. Lett.* **95**(22), 227401 (2005)
5. B. Bai, Y. Svirko, J. Turunen, T. Vallius, *Phys. Rev. A* **76**(2), 023811 (2007)
6. X. Yin, M. Schäferling, B. Metzger, H. Giessen, *Nano Lett.* **13**(12), 6238 (2013)
7. X. Yin, M. Schäferling, A.K.U. Michel, A. Tittl, M. Wuttig, T. Taubner, H. Giessen, *Nano Lett.* **15**(7), 4255 (2015)
8. X. Duan, S. Yue, N. Liu, *Nanoscale* **7**(41), 17237 (2015)
9. S. Zu, Y. Bao, Z. Fang, *Nanoscale* **8**(7), 3900 (2016)
10. V.P. Drachev, W.D. Bragg, V.A. Podolskiy, V.P. Safonov, W.T. Kim, Z.C. Ying, R.L. Armstrong, V.M. Shalaev, *J. Opt. Soc. Am. B* **18**(12), 1896 (2001)
11. T. Narushima, H. Okamoto, *J. Phys. Chem. C* **117**(45), 23964 (2013)
12. T. Narushima, S. Hashiyada, H. Okamoto, *ACS Photonics* **1**(8), 732 (2014)
13. S. Hashiyada, T. Narushima, H. Okamoto, *J. Phys. Chem. C* **118**(38), 22229 (2014)
14. E. Hendry, T. Carpy, J. Johnston, M. Popland, R. Mikhaylovskiy, A. Laphorn, S. Kelly, L. Barron, N. Gadegaard, M. Kadodwala, *Nat. Nanotechnol.* **5**(11), 783 (2010)
15. Y. Tang, A.E. Cohen, *Science* **332**(6027), 333 (2011)
16. A. Kuzyk, R. Schreiber, Z. Fan, G. Pardatscher, E.M. Roller, A. Högele, F.C. Simmel, A.O. Govorov, T. Liedl, *Nature* **483**(7389), 311 (2012)
17. J. Kumar, H. Eraña, E. López-Martínez, N. Claes, V.F. Martín, D.M. Solís, S. Bals, A.L. Cortajarena, J. Castilla, L.M. Liz-Marzán, *Proceedings of the National Academy of Sciences*, p. 201721690 (2018)
18. K. Sakai, T. Yamamoto, K. Sasaki, *Sci. Rep.* **8**(1), 7746 (2018)
19. H. Ishihara, K. Cho, *Phys. Rev. B* **48**(11), 7960 (1993)
20. H. Ishihara, K. Cho, *Solid State Commun.* **89**(10), 837 (1994)
21. H. Ishihara, K. Cho, K. Akiyama, N. Tomita, Y. Nomura, T. Isu, *Phys. Rev. Lett.* **89**(1), 017402 (2002)
22. M. Takase, H. Ajiki, Y. Mizumoto, K. Komeda, M. Nara, H. Nabika, S. Yasuda, H. Ishihara, K. Murakoshi, *Nat. Photonics* **7**(7), 550 (2013)
23. M. Ichimiya, M. Ashida, H. Yasuda, H. Ishihara, T. Itoh, *Phys. Rev. Lett.* **103**(25), 257401 (2009)
24. T. Kinoshita, T. Matsuda, T. Takahashi, M. Ichimiya, M. Ashida, Y. Furukawa, M. Nakayama, H. Ishihara, *Phys. Rev. Lett.* **122**(15), 157401 (2019)
25. M. Hoshina, N. Yokoshi, H. Ishihara, *Opt. Express* **28**(10), 14980 (2020)
26. D. Nowak, W. Morrison, H.K. Wickramasinghe, J. Jahng, E. Potma, L. Wan, R. Ruiz, T.R. Albrecht, K. Schmidt, J. Frommer et al., *Sci. Adv.* **2**(3), e1501571 (2016)
27. P.B. Johnson, R.W. Christy, *Phys. Rev. B* **6**(12), 4370 (1972)
28. E.M. Purcell, C.R. Pennypacker, *Astrophys. J.* **186**, 705 (1973)

29. T. Iida, H. Ishihara, *Phys. Rev. B* **77**(24), 245319 (2008)
30. M. Ternes, C.P. Lutz, C.F. Hirjibehedin, F.J. Giessibl, A.J. Heinrich, *Science* **319**(5866), 1066 (2008)
31. T. Iida, H. Ishihara, *Phys. Rev. Lett.* **97**(11), 117402 (2006)
32. J. Yamanishi, Y. Naitoh, Y. Li, Y. Sugawara, *Phys. Rev. Appl.* **9**(2), 024031 (2018)
33. A. Ashkin, J.M. Dziedzic, J. Bjorkholm, S. Chu, *Opt. Lett.* **11**(5), 288 (1986)
34. L. Allen, M.W. Beijersbergen, R. Spreeuw, J. Woerdman, *Phys. Rev. A* **45**(11), 8185 (1992)
35. A. O'neil, I. MacVicar, L. Allen, M. Padgett, *Phys. Rev. Lett.* **88**(5), 053601 (2002)
36. T. Sugiura, S. Kawata, *Bioimaging* **1**(1), 1 (1993)
37. L. Novotny, R.X. Bian, X.S. Xie, *Phys. Rev. Lett.* **79**(4), 645 (1997)
38. M. Righini, A.S. Zelenina, C. Girard, R. Quidant, *Nat. Phys.* **3**(7), 477 (2007)
39. M.L. Juan, M. Righini, R. Quidant, *Nat. Photonics* **5**(6), 349 (2011)
40. K. Wang, E. Schonbrun, P. Steinvurzel, K.B. Crozier, *Nat. Commun.* **2**(1), 1 (2011)
41. T. Shoji, Y. Tsuboi, *J. Phys. Chem. Lett.* **5**(17), 2957 (2014)
42. P.R. Huft, J.D. Kolbow, J.T. Thweatt, N.C. Lindquist, *Nano Lett.* **17**(12), 7920 (2017)
43. K. Liu, N. Maccaferri, Y. Shen, X. Li, R.P. Zaccaria, X. Zhang, Y. Gorodetski, D. Garoli, *Opt. Lett.* **45**(4), 823 (2020)
44. A.N. Koya, J. Cunha, T.L. Guo, A. Toma, D. Garoli, T. Wang, S. Juodkazis, D. Cojoc, R. Proietti Zaccaria, *Advanced Optical Materials*, p. 1901481 (2020)
45. T. Iida, H. Ishihara, *Opt. Lett.* **27**(9), 754 (2002)
46. R.R. Agayan, F. Gittes, R. Kopelman, C.F. Schmidt, *Appl. Opt.* **41**(12), 2318 (2002)
47. T. Iida, H. Ishihara, *Phys. Rev. Lett.* **90**(5), 057403 (2003). See also, *Phys. Rev. Focus* **11**, Story 6, 11 Feb. (2003)
48. H. Ajiki, T. Iida, T. Ishikawa, S. Uryu, H. Ishihara, *Phys. Rev. B* **80**(11), 115437 (2009)
49. T. Kudo, H. Ishihara, *Phys. Rev. Lett.* **109**(8), 087402 (2012)
50. K. Inaba, K. Imaizumi, K. Katayama, M. Ichimiya, M. Ashida, T. Iida, H. Ishihara, T. Itoh, *physica status solidi (b)* **243**(14), 3829 (2006)
51. H. Li, D. Zhou, H. Browne, D. Klenerman, *J. Am. Chem. Soc.* **128**(17), 5711 (2006)
52. C. Hosokawa, H. Yoshikawa, H. Masuhara, *Jpn. J. Appl. Phys.* **45**(4L), L453 (2006)
53. T. Shoji, N. Kitamura, Y. Tsuboi, *J. Phys. Chem. C* **117**(20), 10691 (2013)
54. S.E.S. Spesyvtseva, S. Shoji, S. Kawata, *Phys. Rev. Appl.* **3**(4), 044003 (2015)
55. Y. Jiang, T. Narushima, H. Okamoto, *Nat. Phys.* **6**(12), 1005 (2010)
56. T. Kudo, H. Ishihara, H. Masuhara, *Opt. Express* **25**(5), 4655 (2017)
57. H. He, M. Friese, N. Heckenberg, H. Rubinsztein-Dunlop, *Phys. Rev. Lett.* **75**(5), 826 (1995)
58. N. Simpson, K. Dholakia, L. Allen, M. Padgett, *Opt. Lett.* **22**(1), 52 (1997)
59. A. Alabastri, S. Tuccio, A. Giugni, A. Toma, C. Liberale, G. Das, F.D. Angelis, E.D. Fabrizio, R.P. Zaccaria, *Materials* **6**(11), 4879 (2013)
60. S. Chu, T. Su, R. Oketani, Y. Huang, H. Wu, Y. Yonemaru, M. Yamanaka, H. Lee, G. Zhuo, M. Lee et al., *Phys. Rev. Lett.* **112**(1), 017402 (2014)
61. H.J. Carmichael, *Statistical Methods in Quantum Optics I: Master Equations and Fokker-Planck Equations* (Springer Science & Business Media, 2013)
62. S. Albaladejo, M.I. Marqués, M. Laroche, J.J. Sáenz, *Phys. Rev. Lett.* **102**(11), 113602 (2009)
63. M.V. Berry, *J. Opt. A: Pure Appl. Opt.* **11**(9), 094001 (2009)